PHOTONICS Research

Lensless Fourier-transform terahertz digital holography for real-time full-field phase imaging

Yaya Zhang,[1,†] Jie Zhao,[1,2,†] Dayong Wang,[1,2,†] Yunxin Wang,[1,2] and Lu Rong[1,2,*]

[1]College of Physics and Optoelectronics, Faculty of Science, Beijing University of Technology, Beijing 100124, China
[2]Beijing Engineering Research Center of Precision Measurement Technology and Instruments, Beijing 100124, China
*Corresponding author: ronglu@bjut.edu.cn

Received 1 July 2021; revised 11 November 2021; accepted 18 November 2021; posted 22 November 2021 (Doc. ID 435769); published 11 January 2022

With the development of continuous-wave terahertz (THz) sources and array detectors, the pursuit of high-fidelity real-time imaging is receiving significant attention within the THz community. Here, we report a real-time full-field THz phase imaging approach based on lensless Fourier-transform THz digital holography. A triangular interferometric layout is proposed based on an oblique illumination of 2.52 THz radiation, which is different from other lensless holographic configurations at other frequencies. A spherical reference beam is generated by a reflective parabolic mirror with minor propagation loss. The complex-valued images are reconstructed using a single inverse Fourier transform of the hologram without complex calculation of the diffraction propagation. The experimental result for a Siemens star validates the lateral resolution of ∼346 μm in the diagonal direction. Sub-pixel image registration and image stitching algorithms are applied to enlarge the area of the reconstructed images. The dehydration process of an aquatic plant leaf (*Hottonia inflata*) is monitored for the first time, to the best of our knowledge, at the THz band. Rapid variations in water content and morphology are measured with a time interval of 0.6 s and a total time of 5 min from a series of reconstructed amplitude and phase images, respectively. The proposed method has the potential to become a powerful tool to investigate spontaneous phenomena at the THz band.

https://doi.org/10.1364/PRJ.435769

1. INTRODUCTION

Terahertz (THz) waves can penetrate diverse non-conducting and optically opaque materials without ionization but are nevertheless strongly absorbed by water molecules and are thus quite suitable for biomedical imaging, materials characterization, and non-destructive testing [1–4]. For samples with low amplitude contrast at the THz band, various phase imaging approaches with different types of sources and layouts have been proposed to reveal the thickness, refractive index, morphology, and internal structure from phase images. Through the utilization of some of these approaches, which use advanced image acquisition and reconstruction strategies, it is possible to achieve real-time imaging [5]. THz pulsed imaging (TPI), which is commonly based on commercial THz time-domain spectroscopy, provides broadband spectral images with both amplitude and phase information [6]. However, it has limited data acquisition speed in the raster scanning mode when using mechanical optical delay lines and THz photoconductive antennas, e.g., ∼1 h for an image of 640 × 480 pixels [7]. This time-consuming acquisition can be addressed to some extent either by adopting asynchronous sampling with a pair of synchronized femtosecond lasers [8] or by using fast rotary prisms [9]. Full-field TPI is achieved by electro-optic sampling, while the signal-to-noise ratio (SNR) is degraded with the absence of lock-in amplifiers, and the field-of-view (FOV) is restrained by the size of non-linear crystals [10,11]. THz single-pixel imaging can effectively squeeze the long acquisition time by using mask coded illumination and compressive sensing sampling [12,13]. The amplitude and phase changes in a leaf of a terrestrial plant have been tracked in a 32 × 32 pixels window during its dehydration process with a rate of 6 frames-per-second (fps) [14]. The acquisition time grows linearly with the expansion of the image size. With heterodyne profilometry, it is possible to scan an area of 80 mm × 80 mm within 30 min and retrieve the complex amplitude distribution using two continuous-wave (CW) THz sources with adjacent frequencies [15]. Laser feedback interferometry (also known as self-mixing interferometry) uses quantum cascade lasers as transceivers for THz reflective phase imaging [16,17]. For these point scanning imaging approaches, mechanical inertia is the bottleneck to further boost the imaging speed.

By virtue of the rapid development in THz array detectors, e.g., microbolometers and pyroelectric detectors, CW THz full-field phase imaging has become the new trend in THz

imaging. The phase can be retrieved from the recorded intensity of diffraction patterns and holograms, e.g., THz ptychography can simultaneously reconstruct both the incident probe distribution and the complex-valued transmission function of a sample's partially overlapped illuminated regions using different recording geometries [18–22]. Successive recording of diffraction patterns guarantees the unique solution and convergence speed of this approach, nevertheless restraining its ability to investigate simultaneous phenomena. CW THz digital holography (TDH) is another lensless full-field phase imaging approach [23–32]. Due to its compact in-line scheme, Gabor TDH provides sub-wavelength lateral resolution [23], while the sample size is restrained for the balance of the scattered object beam and the unscattered reference beam [24]. Furthermore, the suppression of the twin image requires time-consuming iterative phase retrieval algorithms [25]. In phase-shifting TDH, the restriction of the sample size is alleviated due to the additional on-axis reference beam in the Mach–Zehnder architecture [27]. It has limited real-time imaging ability since three or more fixed-step phase-shifting holograms need to be recorded to eliminate the twin image. Common-path self-referencing TDH overcomes this issue by recording the off-axis hologram and performing a subsequent spatial Fourier filtering [28]. The FOV of this robust geometry is approximately half of size of the illumination beam. Off-axis Fresnel TDH achieves dynamic imaging in both reflection (640 × 480 pixels, 5 fps) [29] and transmission modes (320 × 240 pixels, 3.5 fps) [30]. Either Fresnel–Kirchoff or angular spectrum integral is adopted for the diffraction propagation calculation depending on the reconstruction distance. The essential numerical focusing is often time-consuming. Currently, the potential of real-time phase imaging in TDH has not yet been fully released.

Lensless Fourier-transform holography (LFH) is another prosperous real-time phase imaging approach that has been validated at other bands, e.g., the soft X-ray, extreme ultraviolet (EUV), and visible-light regime [33–38]. The object beam interferes with the diverging reference beam with the same spherical curvature. The hologram is a sinusoidal fringe of a vector spatial frequency, which makes the most efficient use of the space bandwidth product of the detector [33]. Numerical reconstruction requires a single inverse Fourier transform without additional diffraction propagation, thus providing phase information in almost real-time. To offset the quadratic phase factor, the reference beam is brought to focus at the object plane and is equidistant from the recording plane. The Mach–Zehnder configuration with the intervention of a beam splitter between the sample and the detector is widely adopted in the visible-light domain, but it is too bulky for TDH. Extended recording distance would lead to the decreased lateral resolution in the latter case. In the case of no beam splitter, e.g., the soft X-ray and EUV, an object mask with a pinhole generates a common-path divergent reference beam. The transmission energy would have considerable loss if a mask or a transmissive lens is adopted for THz imaging.

In this study, we propose an off-axis triangular LFH geometry based on oblique illumination and apply it to THz real-time full-field phase imaging. A parabolic mirror (PM) is adopted to generate a spherical reference beam. Successive reflections are suppressed by the triangular layout. The experimental lateral resolution is evaluated using a gold-plated Siemens star. The size of the reconstructed images can be expanded through sub-pixel image registration and image stitching. Finally, the dehydration process of an aquatic leaf is quantitatively monitored.

2. METHODS

The schematic diagram of the lensless Fourier-transform TDH (LF-TDH) is shown in Fig. 1. Both the object and the point source of the reference beam are placed at the x_0–y_0 plane. The incident angle of the planar illumination beam is assumed to be θ. The array detector is located at the recording plane, which is parallel to the object plane and denoted as the x–y plane. The center of the detector aligns with the center of the illumination beam, and thus is $d\ \tan\theta$ away from the coordinate center at the recording plane, where d denotes the vertical distance between the object plane and the recording plane. In the proposed triangular configuration, both the object wavefront along the inclined illumination direction and the reference beam can be expressed under the paraxial approximation within the detector, even if the angles α and θ are not very small practically.

We assume $u(x_0, y_0)$ is the complex amplitude at the object plane. Under the Fresnel approximation, the object wavefront at the recording plane can be simplified as [39]

$$\begin{aligned} O(x,y) &\propto \exp\left[\frac{jk}{2d}(x^2+y^2)\right] \\ &\times \iint_{-\infty} u(x_0,y_0)\exp\left(j2\pi\frac{\sin\theta}{\lambda}x_0\right) \\ &\times \exp\left[\frac{jk}{2d}(x_0^2+y_0^2)\right]\exp\left[-\frac{jk}{d}(xx_0+yy_0)\right]\mathrm{d}x_0\mathrm{d}y_0 \\ &\propto \exp\left[\frac{jk}{2d}(x^2+y^2)\right]U\left(\frac{x-d\ \sin\theta}{\lambda d},\frac{y}{\lambda d}\right), \end{aligned} \tag{1}$$

with

$$U(p,q) = \Im\left\{u(x_0,y_0)\exp\left[\frac{jk}{2d}(x_0^2+y_0^2)\right]\right\}\Big|_{p=\frac{x}{\lambda d},q=\frac{y}{\lambda d}}, \tag{2}$$

where λ is the wavelength, k represents the wave number, and $k = 2\pi/\lambda$. $\Im\{\}$ denotes the Fourier transform. The divergent reference beam can be formulated as follows:

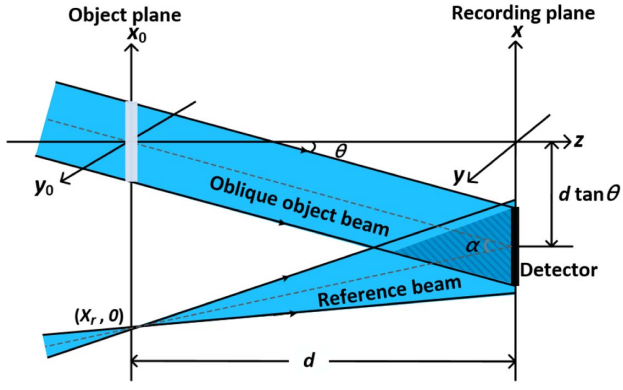

Fig. 1. Schematic of LF-TDH coordinate system.

$$R(x,y) \propto \exp\left[\frac{jk}{2d}(x^2+y^2)\right]\exp\left(\frac{jk}{d}xx_r\right), \quad (3)$$

in which $(x_r, 0)$ is the coordinate of the point source of the reference beam. The reference beam interferes with the object beam with an off-axis angle of α. The hologram can be expressed as

$$I(x,y) = |O+R|^2 = |O|^2 + |R|^2 + O^*R + OR^*, \quad (4)$$

where * denotes the complex conjugate. In the proposed geometry, the incident angle θ is around half of the off-axis angle α and does not need to be accurately measured. Meanwhile, the effect of the spherical phase factor associated with Fresnel diffraction is eliminated. The fourth term of the right-hand side of Eq. (4) can be simplified as

$$O(x,y)R^*(x,y) \propto U\left(\frac{x - d\ \sin\theta}{\lambda d}, \frac{y}{\lambda d}\right)\exp\left(-\frac{jk}{d}xx_r\right). \quad (5)$$

It is noted that a linear phase shift of $\sin\theta/\lambda$ in the frequency domain is equivalent to a translation of $d\ \sin\theta$ in the space domain [39]. Considering the orientation of the detector in this geometry, the center of the hologram coincides with the center of the Fourier transform, which inherently offsets the phase shift from the oblique illumination. It is noted that as long as the angle θ is smaller than or equal to 15°, the value of $\sin\theta$ is close to the value of $\tan\theta$ with the relative error below 4%, which can be reasonably negligible. Let us use the coordinates (x_1, y_1), denoting the location where the detector is placed, where $x_1 = x - d\ \sin\theta$ and $y_1 = y$, so that Eq. (5) becomes

$$O(x_1,y_1)R^*(x_1,y_1) \propto U\left(\frac{x_1}{\lambda d}, \frac{y_1}{\lambda d}\right)\exp(jk\ \sin\theta x_r)\exp\left(-\frac{jk}{d}x_1x_r\right), \quad (6)$$

where the first exponential term in Eq. (6) is a constant term that can be omitted in the phase image, while the second exponential term is a linear phase factor that is going to be accounted for when the order of u_{+1} is cropped in the reconstructed image. The real image can be reconstructed using a single inverse Fourier transform $\mathfrak{F}^{-1}\{\}$ of the hologram:

$$u_{+1}(x_0,y_0) = \mathfrak{F}^{-1}\{O(x_1,y_1)R^*(x_1,y_1)\} \propto u(x_0 - x_r, y_0)\exp\left[\frac{jk}{2d}(x_0 - x_r)^2 + y_0^2\right]. \quad (7)$$

Meanwhile, the DC term $u_0(x_0,y_0) = \mathfrak{F}^{-1}\{|O|^2 + |R|^2\}$ locates at the center of the reconstructed object image, and the twin image $u_{-1}(x_0,y_0) = \mathfrak{F}^{-1}\{O^*R\}$ is placed in $(-x_r, 0)$, which is centrosymmetric to the real image. With a proper distance x_r and certain off-axis angle α, the real image is not superposed with the DC term and the twin image.

The double exposure method [40] is used to compensate for the additional quadratic phase factor in Eq. (7). The corrected phase is obtained by subtracting the phase distribution, which is reconstructed from a background hologram. This hologram is recorded using identical experimental parameters without the sample. Phase unwrapping is subsequently conducted if necessary by using the least squared method [41]. Theoretically, this method is also available for correcting phase aberration [42], which is not adopted because the reconstruction quality is not as good as the double exposure method in our reconstruction.

3. EXPERIMENTAL RESULTS

A. Experimental Setup

The diagram of the experimental setup is depicted in Fig. 2. A far-infrared CO_2 laser pumped CH_3OH vapor to emit a CW THz beam (295-FIRL-HP, Edinburgh Instruments) at a wavelength of 118.83 μm (2.52 THz) with a maximum output power of up to 500 mW. The diameter of the emitted beam was ~7 mm. It was expanded to 22 mm in diameter using two gold-coated off-axis PMs, PM_1 and PM_2, with effective focal lengths of 50.8 mm and 152.4 mm, respectively. The collimated beam was partitioned into two beams by an HRFZ-Si beam splitter ($n = 3.4287$ at 2.5197 THz), the diameter and the thickness of which are 50.8 mm and 3 mm, respectively. The splitting ratio between the transmissive beam and the reflective beam was 54%:46%. The reflective portion went through the thin sample and generated the object beam. Another beam was reflected by PM_3 with an off-axis angle of 60° and became a spherical reference beam with a focal length of 101.6 mm. The off-axis angle α between the object beam and reference beam was ~26.5°.

LF-TDH holograms were recorded by a pyroelectric detector (Pyrocam IV, Ophir-Spiricon, Inc.), with a pixel pitch of 80 μm × 80 μm featuring 320 × 320 pixels. Because CW THz beams must be chopped to create a changing signal, the detector contains an integrated chopper before the sensor. The chopping frequency was set to 50 Hz. To enhance the contrast of the holographic fringes, multiple frames were accumulated for each hologram. The accumulation numbers are different in the following experiments. In our imaging system, the Fresnel number was 4.48, so it could be considered that the detector was located in the Fresnel diffraction zone [39]. It is noted that the point source of the reference beam has to be placed at the object plane. An auxiliary thermal sensitive plate was placed next to the sample at the object plane blocking the path of the reference beam. Once the point source was on the plate, a tiny hole was burnt by the converging reference beam. Meanwhile, the reconstructed image would be out of focus if the point source and the sample were not on the same plane. The distance d was ~72 mm, which was the same for the following experiments.

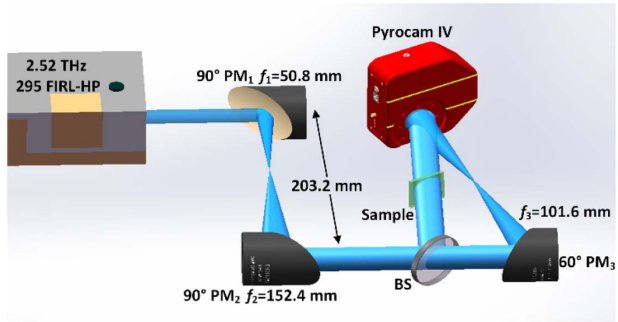

Fig. 2. Schematic of LF-TDH experimental layout.

B. Reconstruction Results

1. Resolution of Reconstructed Amplitude Image

To determine the spatial resolution of the LF-TDH setup, a Siemens star with an outer diameter of 20 mm was adopted. A photograph of the sample is given in Fig. 3(a). The sample had a spoke angle of 7.5° and a total of 48 spokes. The opaque spokes were fabricated by sputtering an Au coating on a high-resistivity float zone Si (HRFZ-Si) substrate via photolithography. The thicknesses of the substrate and Au coating are 500 μm and 50 nm, respectively. The resolutions at the outer diameter and the center circle of this target are 0.38 and 7.66 lp/mm, respectively. The illuminated region of the sample is inside the white dashed-line box in Fig. 3(a). For the reconstruction, 500 frames were recorded and accumulated via Gaussian fitting to be a synthesized hologram [25]. Figure 3(b) shows the accumulated hologram. The fringe contrast is the metric to evaluate the quality of the hologram [43], the value of which is 0.682, as shown in the red rectangle in Fig. 3(b).

Figure 3(c1) shows the reconstructed amplitude image of the object after an inverse Fourier transform of the hologram. For better display, it was resized from the original 320 × 320 pixels into 1200 × 1200 pixels by the nearest interpolation method. This approach was adopted for the other two samples. It can be seen that the zero-order image occupies too much energy, which leads to blurred details in the real image. The Laplacian filter was applied to the hologram to filter out the DC term [44], and the result is shown in Fig. 3(c2). It is noted that the Tukey window function was multiplied by the filtered hologram to suppress the negative influence of the aperture diffraction [45]. The cropped region illustrated as the red-line box in Fig. 3(c2) is 220 × 220 pixels.

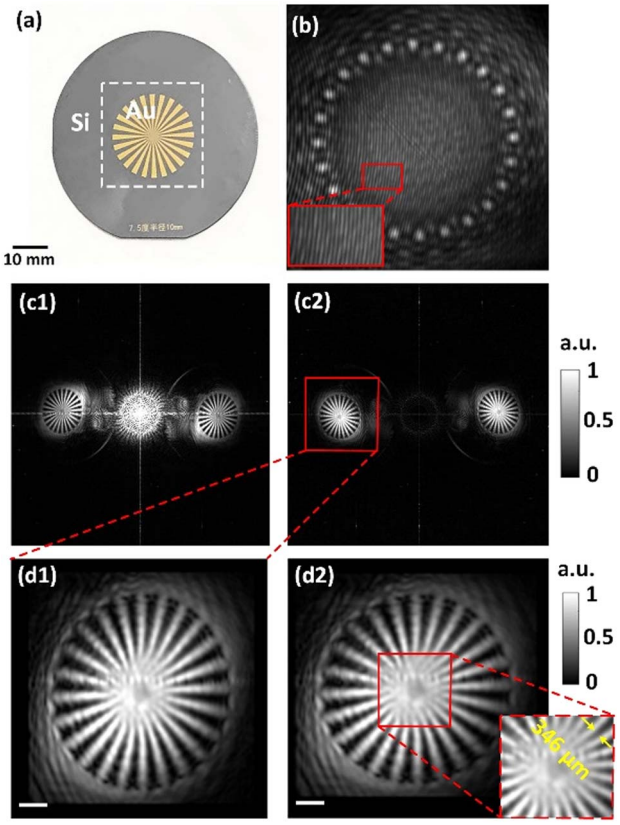

Fig. 3. Siemens star and its LF-TDH reconstruction results. (a) Photograph of the sample. (b) Accumulated hologram of 500 frames. (c1) Reconstructed amplitude image after a single inverse Fourier transform of (b). (c2) Reconstructed amplitude image after DC term filtering and apodization from (c1). (d1), (d2) The reconstructed amplitude images before and after correction, respectively. White scale bars represent 3 mm.

In this experiment, the gold-coated sample has high reflectivity and fine features. To further suppress the minor residual successive reflections, it was not perfectly parallel to the detector. Therefore, the distortion known as anamorphism should be considered. It is shown in Fig. 3(d1) that the aspect ratio of the length to the width in the reconstructed Siemens star was 1.43. The anamorphism was numerically corrected by adopting a tilted plane correction method [21]. The results can be seen in Fig. 3(d2). Theoretically, the lateral resolution is anisotropic due to the rectangular detector. The highest resolution was $\delta = \lambda d/\sqrt{2}M\Delta x = 236$ μm in the diagonal direction [39], where M and Δx are the pixel number and pitch, respectively. It is illustrated in the enlarged sub-image of Fig. 3(d2) that the experimental resolution was ∼346 μm in the diagonal direction.

2. Wide-Field Phase Imaging by Image Stitching

It is illustrated in Fig. 4(a) that a polypropylene (PP) plate patterned with letters was adopted as the sample. The length and width of the patterned region are ∼45 mm and ∼5 mm, respectively. The thickness of the patterned and unpatterned areas of the plate was measured to be ∼411 μm and ∼337 μm by a screw-thread micrometer, respectively. The absorption coefficient and the refractive index are ∼3.9 cm^{-1} [46] and 1.5151 at 2.5197 THz (TeraPulse-4000, TeraView), respectively. The sample was mounted parallel to the detector. The influence of the non-uniform illumination of the THz beam on the fidelity of reconstruction cannot be neglected. To suppress this effect, two holograms in the presence and absence of the object were recorded and reconstructed, separately. Each hologram was accumulated by 500 frames via Gaussian fitting [25]. Theoretically, the amplitude difference with or without the embossed letters is ∼1.5%, and thus this PP plate can be categorized as a pure phase object. However, the letters can be clearly recognized in both the amplitude and phase images. There are two possible reasons to explain the mechanism of the silhouette in the reconstructed amplitude images. First, LF-TDH is sensitive to the thickness difference of the sample, i.e., the defocused regions. Second, THz waves have stronger diffraction effect than the coherent visible light due to the much longer wavelength. The cut-profile in Fig. 4(b4) represents clear edges of the embossed pattern and the plate. The mean phase difference between the patterned and unpatterned areas was ∼2.47 rad, and the corresponding thickness was ∼78 μm with relative error of 5.4%.

The effective FOV of this layout, restrained by the size of the illumination beam, was approximately 22 mm × 22 mm. It was not sufficient for the whole sample width. Therefore, the sample was mounted on a motorized two-axis translation stage (LTS300, Thorlabs). It was scanned along the x axis in steps of

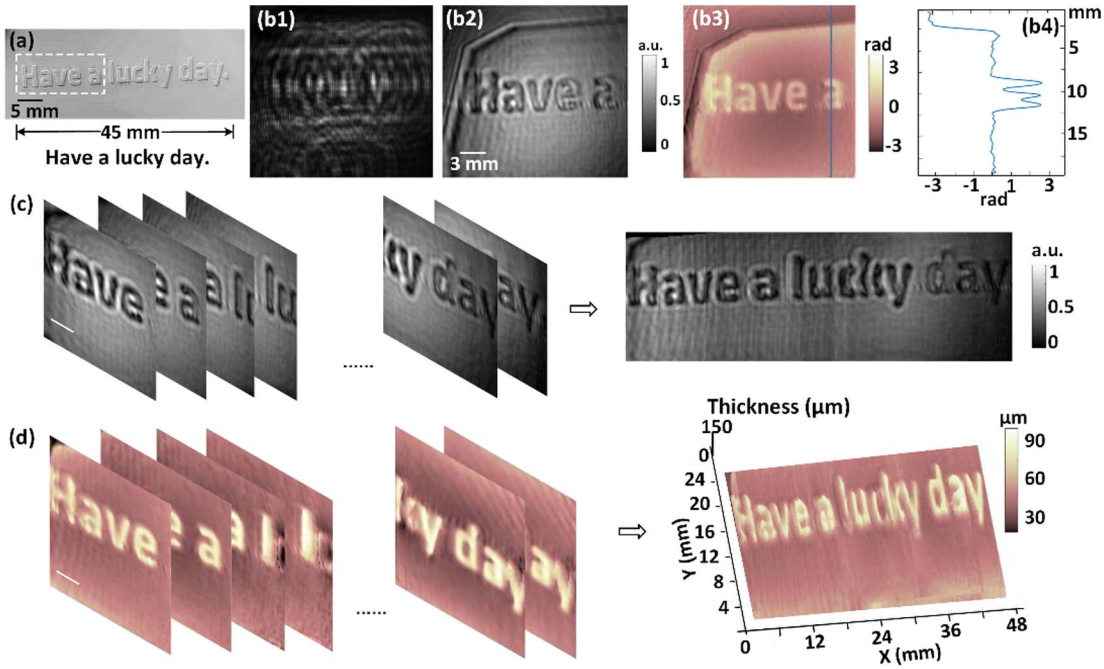

Fig. 4. LF-TDH reconstruction results of a PP plate. (a) Photograph with schematic pattern. (b1)–(b3) Hologram, the corresponding reconstructed amplitude and phase images, respectively. (b4) The cut-profile of the blue line plotted in (b3). (c) Expanded amplitude distribution by stitching 20 images. (d) The 3D thickness profile distribution of the sample by stitching unwrapped phase images.

1.65 mm to ensure that the adjacent positions had an area overlapping ratio of ∼85%. To obtain complete distribution of the object, sub-pixel image registration [47] and image stitching [31] algorithms were adopted after the reconstruction of the individual holograms. First, the relative transverse displacement of adjacent reconstructed images was calculated between the overlap region, which is necessary for image registration and intensity correction [47]. Second, the section images were stitched to form the expanded image. After that, the weighted smoothness was utilized to reduce the stitching error. The enlarged amplitude and phase images synthesized by 20 individual images are illustrated in Figs. 4(c) and 4(d), respectively. The image width was expanded from 18.3 mm to 44.2 mm, which was two times larger than the effective FOV.

3. Real-Time Measurement of Leaf Dehydration

Leaves are the main organ of photosynthesis and transpiration in plants. The changes in their water contents indicate the physiological status of plants. Different from commonly used destructive methods, e.g., gravimetry, THz spectroscopy and imaging have been validated for non-invasively quantifying the water contents of leaves [14,48–52]. Compared with terrestrial herbaceous plants, aquatic leaves have higher water contents, which dehydrate much more rapidly after leaving the water environment. A leaf of *Hottonia inflata* was selected as the sample and mounted on a 3-mm-thick quartz slide, which was parallel to the detector. It is shown in Fig. 5(a1) that this aquatic leaf has 11 pinnate deep-parted alternate leaflets. The image shows the leaf veins with a submillimeter resolution, which are responsible for the delivery of water and dissolved nutrients. Frames were recorded successively at a chopping frequency of 50 Hz for 300 s. A photograph of the dehydrated leaf after data acquisition is shown in Fig. 5(a2).

Considering the rapid dehydration process of the aquatic leaf, each hologram was obtained by accumulating 30 frames without Gaussian fitting, since 30 frames are statistically insufficient to extract the expectancy of the intensity from the Gaussian statistics. Therefore, the time interval of the adjacent holograms was 0.6 s. The computational time for the complete reconstruction of each hologram, on a desktop personal computer (PC) with 3.4 GHz i5-7500, 8 GB random access memory (RAM), and R2016B MATLAB, was 0.187 s, which is ∼1/3 of the time interval of the successive holograms. The calculation includes the inverse Fourier transform and other processing steps, e.g., interpolation, Laplacian filtering, apodization, phase aberration correction, and phase unwrapping. It is noted that anamorphism correction is unnecessary, since the sample was mounted parallel to the detector.

Several reconstructed amplitude and phase images were extracted at an interval of 40 s, as shown in Figs. 5(b) and 5(c). Obviously, the morphology of the leaf at the initial moment was distinctly different from that in the final moment. At $t = 81$ s, there was no sign of a droplet attached to the leaf. The contrast of the amplitude image was primarily generated from the transmittance difference due to the water content in the main and minor veins. At $t = 161$ s, it is clearly shown in Fig. 5(b) that the absorption of THz radiation by the tips and margins of leaflets was significantly reduced, indicating that the leaf was in a dehydrated state. At $t = 281$ s, the amplitude image shows that the tips and margins of the leaflets had higher THz transmission than the leaf main vein. In contrast, the phase distribution at that moment was clearer than at the other

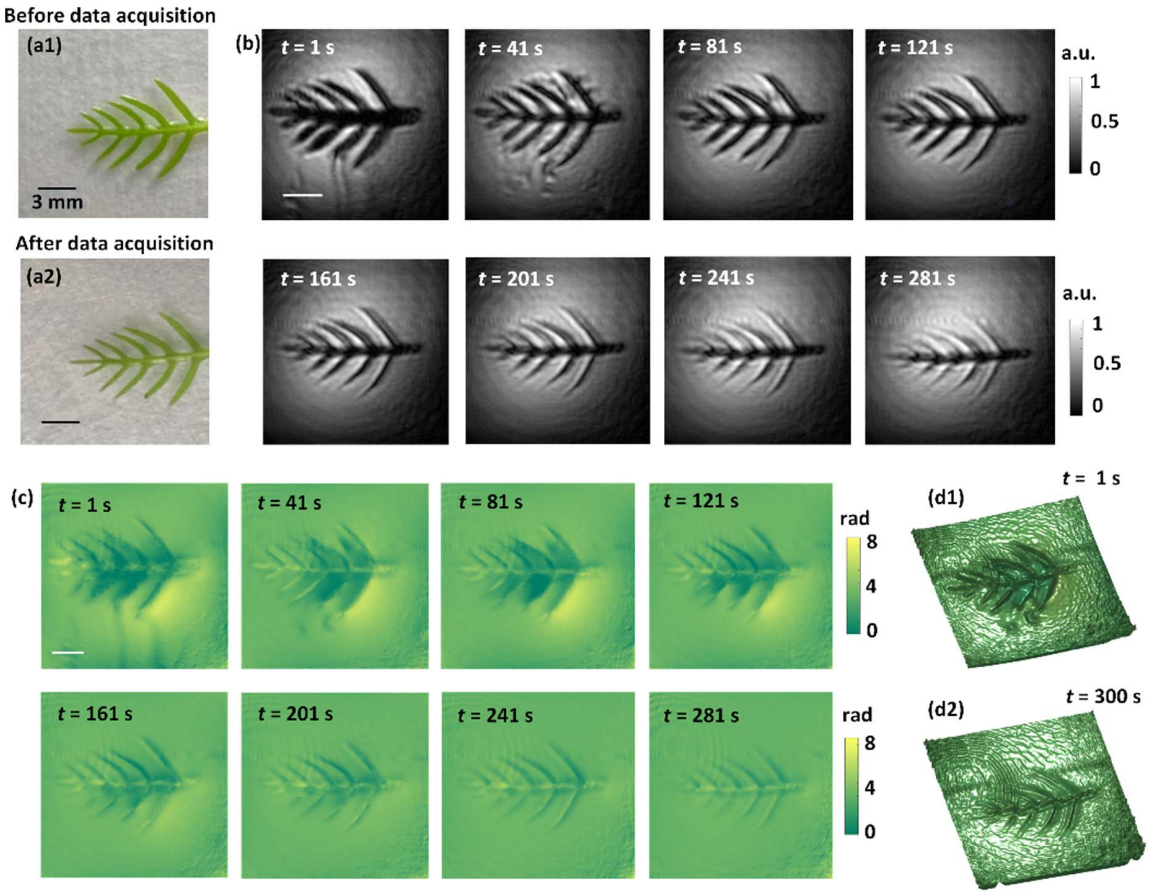

Fig. 5. Dynamic observation results of an aquatic leaf (*Hottonia inflata*) based on LF-TDH. Photographs of the leaf (a1) before and (a2) after data acquisition. Reconstructed (b) amplitude and (c) phase results. The 3D profile distributions at (d1) the begining and (d2) the end of data acquisition. Black and white scale bars represent 3 mm.

moments. It is known that the unwrapped phase reflects the morphology of the leaf. During dehydration, the thickness of the leaf became smaller. The dynamic change process of 500 successive images with a time interval of 0.6 s can be viewed in the video (Visualization 1). The evaporation of the water surrounding the leaf can be seen in Visualization 1, which changed the focusing position and blurred the images at the initial moments. Figures 5(d1) and 5(d2) reveal that the water content of the leaf decreased distinctly, which is due to the chloroplasts contained inside the cell collapsing and reducing the leaf thickness [53]. Further analysis of the change in water content and its calculation using the Lambert–Beer attenuation law can be seen in Appendix A, where the whole leaf as well as its small parts, i.e., the leaf tip, the rachis, and the area where a leaflet connects to the rachis, is investigated and compared.

4. DISCUSSION AND CONCLUSION

We proposed LF-TDH, in which a triangular geometry based on tilted illumination was built. Similar to other TDH approaches based on CW THz sources and array detectors, e.g., in-line TDH and off-axis Fresnel TDH, LF-TDH is a full-field phase imaging approach. However, unlike these TDH approaches, the complex calculation of diffraction propagation is replaced by a single inverse Fourier transform of the hologram so that the speed of reconstruction is obviously accelerated. The proposed layout is different from other lensless holographic geometries at other frequencies. Compared with current lensless Fourier-transform digital holographic layouts, the proposed layout not only avoids drilling holes at the object mask and wasting THz radiation, but also simplifies the interference architecture and squeezes the recording distance for attainable high resolution. In this system, both the object and recording planes are not perpendicular to the optical axis, the emergent beam from the sample was reflected to the opposite direction by the sensor of the detector, and *vice versa*. Therefore, successive reflections between the object and the detector known as the Fabry–Perot effect can be greatly suppressed. If the object is not parallel to the detector, e.g., the Siemens star, a tilted plane correction method is needed with a frequency spectrum coordinate transformation.

The theoretical and experimental lateral resolutions of the proposed geometry are 236 μm and 346 μm, respectively. The pixel pitch of the THz array detector, i.e., microbolometers and pyroelectric detector, is smaller than the wavelength of the THz beam. Therefore, the aperture of the detector rather than the pixel pitch is the bottleneck of the lateral resolution of

LF-TDH. The use of synthetic aperture is worthy of being investigated to enhance the resolution. Sub-pixel registration and the stitching of overlapped reconstructed images is an effective method to expand the image size. The time interval of temporal adjacent reconstructed images was 0.6 s, while the data acquisition speed, i.e., the chopping frequency of the detector, was 50 Hz. Currently, the bottleneck for the time resolution is the low SNR of the single-frame hologram. For quantitative phase imaging, 30 frames were the minimum accumulation number to get a synthesized THz digital hologram with good fringe contrast. The speed can be easily boosted by replacing the pyroelectric detector with a microbolometer. Both the radiation power fluctuation of the THz laser and the uneven distribution of the THz illumination beam had a negative influence on the fidelity of the individual reconstruction images and the synthesized ones. An appropriate THz spatial filter will help to produce a uniform Gaussian beam.

In summary, LF-TDH has a compact and robust lensless recording layout and simplified reconstruction procedure. Full-field amplitude and phase images can be reconstructed simultaneously. Although the study of dehydration of terrestrial plant leaves is not new at THz frequencies, dynamic detection of an aquatic leaf undergoing rapid dehydration is realized at the THz band for the first time, to the best of our knowledge. The proposed approach is capable of measuring the water variations on the order of sub-seconds in different parts of the leaf from successive amplitude images. When the leaf becomes more transparent to the THz radiation during its dehydration, the changes of the morphology are still clearly revealed by a series of reconstructed phase images. This method provides unprecedented insights into the water dynamics of plants and renders wide applications in THz biomedical imaging. It is noted that the natural evaporation process of the leaf moisture cells may be accelerated by the strong CW THz radiation, which was ~0.284 mW/mm^2. With the development of high-power THz sources, the thermal effect of THz waves should be considered for biomedical imaging. Our future work will involve the calculation of the absolute water content values of the leaf as well by establishing an acropetal mass transport model for water.

APPENDIX A

1. Analysis of Leaf Water Content Changes

The hydration change of the leaf is numerically investigated and compared. It is shown in Fig. 6(a) that three leaf tips (yellow, red, and blue rectangles), a rachis (pink rectangle), and an area where the leaflet connects to rachis (purple rectangle) are chosen. The whole observation time is 300 s, which is made up of 500 accumulated holograms at an interval of 0.6 s. Each hologram is synthesized by 30 frames with a chopping frequency of 50 Hz. Visualization 1 shows that the leaf moves within the FOV as the water evaporates. Meanwhile, it can be seen in Figs. 5(a1) and 5(a2) that the decreased area of the leaf is very small. Therefore, a fixed mask was generated to calculate the variations of the amplitude and phase of the whole leaf and its small parts. Assuming the leaf, i.e., the mask, moved at a constant speed in a certain direction, several points in the main vein of the leaf, illustrated as the black dots in Fig. 6(a),

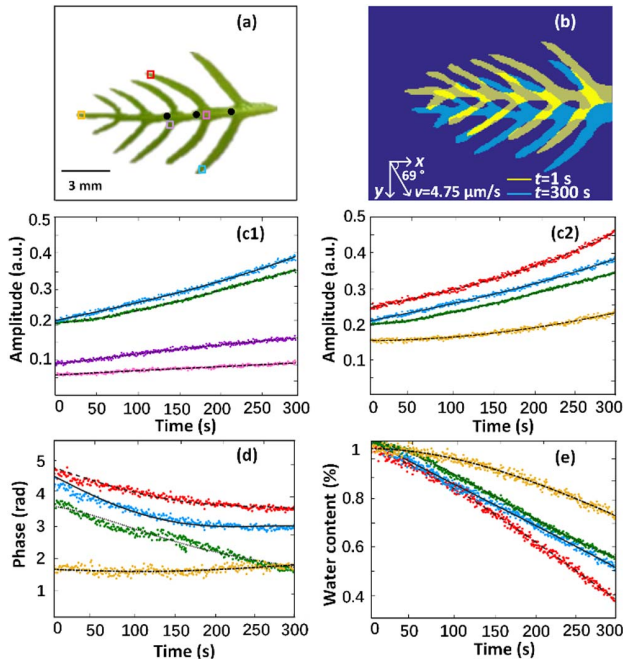

Fig. 6. (a) Reference points (black dots) and different-colored rectangular regions are chosen to estimate (b) the movement of leaf of *Hottonia inflata* and to represent the changes of (c1), (c2) amplitude, (d) phase, and (e) water content under the illumination of 2.52 THz CW beam. The colored dots represent experimental data, and the black lines represent the fitting results. The green curves are the mean values on the full leaf.

were chosen as the reference points to estimate the direction and the velocity of the movement, which were −69° to the lower-right corner and 4.75 μm/s, respectively. The positions of the masks at $t = 1$ s and $t = 300$ s are illustrated in Fig. 6(b).

The amplitude curves of these representative parts and the whole leaf are plotted in Fig. 6(c). The approach of the three-order polynomials was chosen for curve fitting. The blue curve indicates that the leaf tip had a lower water content than the other parts. The average amplitude value increased from 0.200 to 0.387 after 5 min, which is an increment of 93.5% relatively from its original value. The purple curve in Fig. 6(c1) represents the area of contained veins and a small amount of mesophyll tissue. The relative amplitude increment after 5 min was 76.8% (from 0.082 to 0.145). The rachis is located at the axial position of the common petiole. It is the channel where the water and inorganic salts dissolved in the water are transported to the mesophyll cells. The pink curve indicates that the amplitude increment of the rachis was 107% (from 0.057 to 0.118). The mean values inside the moving mask were adopted to plot the green curve representing the average amplitude of the overall leaf, the variation of which was 74.4% (from 0.199 to 0.347) after 5 min. After a small plateau within 40 s, the rising slope of the green curve is similar to the leaf tip (blue curve), but is more pronounced than those of the connection area (purple curve) and the leaf rachis (pink curve). The correlation coefficients between the experimental data and the fitting curves were 0.98–0.99.

Through the analysis above, it is noted that the absolute amplitude variation of the leaf tip (blue region) was more pronounced than in other parts of this leaf. Three leaflet tips are selected for further analysis. The changes of the average amplitude and phase in these three parts are illustrated in Figs. 6(c2) and 6(d), respectively. The amplitude of the terminal leaflet tip represented by the yellow curve was 57.2% (from 0.145 to 0.228). The yellow amplitude and phase curves are flatter than the red and blue ones because the terminal leaflet connected to the rachis and held more water content than the other leaflets in the leaf. Only the yellow phase curve is not monotonous, which might due to the coherent noise. For comparison, the relative amplitude increments of the blue and red curves were 95.4% (from 0.198 to 0.387) and 97.5% (from 0.237 to 0.467), while the relative phase decrements of these two curves were 27.6% (from 4.60 to 3.33 rad) and 23.4% (from 4.75 to 3.64 rad), respectively. It can be found from Fig. 6(d) that the phase value of the whole leaf decreased gradually over time, which is consistent with the optical thickness change shown in Figs. 5(d1) and 5(d2).

2. Calculation of Leaf Water Content

This method relies on the assumption that the absorption of 2.52 THz radiation by the leaf was mainly due to water absorption. The variation of THz transmittance reflects the changes in water content. The Lambert–Beer attenuation law is an effective approach to calculate the water content [54]. The basic idea is to assume that the surface of the leaf is composed of aggregated small squares, which can minimize the influence of volume decreases on the computational accuracy of the water content variation [54]. When the THz radiation passes through each unit, the amplitude change can be expressed as $c = s^2[\ln(I_1/I_0)]/C_0$, where c is the water content, s is the length of the squares, I_1 represents the intensity of THz radiation after penetrating the sample, I_0 comes from an acquisition without the leaf on the 3-mm-thick quartz slide, and C_0 is the absorption coefficient of the sample, which is $28.0 \pm 1.0\ \mathrm{mm}^{-1}$ at 2.52 THz [52]. The slide length of the squares is 3 pixels extracted from the 808×808 pixels reconstructed amplitude images, which are resized by the nearest interpolation method based on the 202×202 pixels reconstructed images illustrated in Fig. 5(b). Therefore, the physical length is ~67 μm, corresponding to one fifteenth of the theoretical resolution along the horizontal direction.

The whole leaf (green curve) and three tips are chosen to plot the decreasing curves of water content in Fig. 6(e). The curves are relative to their beginning and normalized to 100% at $t = 1$ s. It is illustrated in the yellow curve that the water content of the terminal leaflet tip decreased by 25.9% after 5 min, while the red and blue ones declined by 58.5% and 49.1%, respectively. The water content variation of the whole leaf, as illustrated in the green curve, was 45.3% after 5 min. Despite the redistribution of the water content in the leaf, it is plotted as the green curve in Fig. 6(e) that the total trend of the whole leaf descended monotonously. In summary, the validity of monitoring the real-time changes of water content of aquatic leaves is effectively demonstrated.

Funding. National Natural Science Foundation of China (62075001, 62175004); Beijing Municipal Commission of Education (KZ202010005008).

Disclosures. The authors declare no conflicts of interest.

Data Availability. Data underlying the results presented in this paper are not publicly available at this time but may be obtained from the authors upon reasonable request.

[†]These authors contributed equally to this work.

REFERENCES

1. D. M. Mittleman, "Twenty years of terahertz imaging [Invited]," Opt. Express **26**, 9417–9431 (2018).
2. D. Alves-Lima, J. Song, X. Li, A. Portier, Y. Shen, J. A. Zeitler, and H. Lin, "Review of terahertz pulsed imaging for pharmaceutical film coating analysis," Sensors **20**, 1441 (2020).
3. S. Zhong, "Progress in terahertz nondestructive testing: a review," Front. Mech. Eng. **14**, 273–281 (2019).
4. Y. Zhang, C. Wang, B. Huai, S. Wang, Y. Zhang, D. Wang, L. Rong, and Y. Zheng, "Continuous-wave THz imaging for biomedical samples," Appl. Sci. **11**, 71 (2021).
5. H. Guerboukha, K. Nallappan, and M. Skorobogatiy, "Toward real-time terahertz imaging," Adv. Opt. Photon. **10**, 843–938 (2018).
6. J. Coutaz, F. Garet, and V. P. Wallace, *Principles of Terahertz Time-Domain Spectroscopy* (Jenny Stanford, 2018).
7. https://www.menlosystems.com/products/thz-time-domain-solutions/tera-image-3/.
8. A. Bartels, R. Cerna, C. Kistner, A. Thoma, F. Hudert, C. Janke, and T. Dekorsy, "Ultrafast time-domain spectroscopy based on high-speed asynchronous optical sampling," Rev. Sci. Instrum. **78**, 035107 (2007).
9. H. Guerboukha, A. Markov, H. Qu, and M. Skorobogatiy, "Time resolved dynamic measurements at THz frequencies using a rotary optical delay line," IEEE Trans. Terahertz Sci. Technol. **5**, 564–572 (2015).
10. Q. Wu, T. D. Hewitt, and X.-C. Zhang, "Two-dimensional electro-optic imaging of THz beams," Appl. Phys. Lett. **69**, 1026–1028 (1996).
11. L. Guo, X. Wang, P. Han, W. Sun, S. Feng, J. Ye, and Y. Zhang, "Observation of dehydration dynamics in biological tissues with terahertz digital holography [Invited]," Appl. Opt. **56**, F173–F178 (2017).
12. L. Olivieri, J. S. T. Gongora, L. Peters, V. Cecconi, A. Cutrona, J. Tunesi, R. Tucker, A. Pasquazi, and M. Peccianti, "Hyperspectral terahertz microscopy via nonlinear ghost imaging," Optica **7**, 186–191 (2020).
13. S. Chen, L. Du, K. Meng, J. Li, Z. Zhai, Z. Li, and L. Zhu, "Terahertz wave near-field compressive imaging with a spatial resolution of over λ/100," Opt. Lett. **44**, 21–24 (2018).
14. R. I. Stantchev, X. Yu, T. Blu, and E. Pickwell-MacPherson, "Real-time terahertz imaging with a single-pixel detector," Nat. Commun. **11**, 2535 (2020).
15. H. Yuan, D. Voß, A. Lisauskas, D. Mundy, and H. G. Roskos, "3D Fourier imaging based on 2D heterodyne detection at THz frequencies," APL Photon. **4**, 106108 (2019).
16. Y. L. Lim, K. Bertling, T. Taimre, T. Gillespie, C. Glenn, A. Robinson, D. Indjin, Y. Han, L. Li, E. H. Linfield, A. G. Davies, P. Dean, and A. D. Rakić, "Coherent imaging using laser feedback interferometry with pulsed-mode terahertz quantum cascade lasers," Opt. Express **27**, 10221–10233 (2019).
17. M. Wienold, T. Hagelschuer, N. Rothbart, L. Schrottke, K. Biermann, H. T. Grahn, and H. W. Hübers, "Real-time terahertz imaging through self-mixing in a quantum-cascade laser," Appl. Phys. Lett. **109**, 11102 (2016).
18. L. Valzania, T. Feurer, P. Zolliker, and E. Hack, "Terahertz ptychography," Opt. Lett. **43**, 543–546 (2018).
19. L. Rong, C. Tang, D. Wang, B. Li, F. Tan, Y. Wang, and X. Shi, "Probe position correction based on overlapped object wavefront

cross-correlation for continuous-wave terahertz ptychography," Opt. Express **27**, 938–950 (2019).
20. D. Wang, B. Li, L. Rong, F. Tan, J. J. Healy, J. Zhao, and Y. Wang, "Multi-layered full-field phase imaging using continuous-wave terahertz ptychography," Opt. Lett. **45**, 1391–1394 (2020).
21. L. Rong, C. Tang, Y. Zhao, F. Tan, Y. Wang, J. Zhao, D. Wang, and M. Georges, "Continuous-wave terahertz reflective ptychography by oblique illumination," Opt. Lett. **45**, 4412–4415 (2020).
22. L. Rong, F. Tan, D. Wang, Y. Zhang, K. Li, J. Zhao, and Y. Wang, "High-resolution terahertz ptychography using divergent illumination and extrapolation algorithm," Opt. Laser Eng. **147**, 106729 (2021).
23. Z. Li, Q. Yan, Y. Qin, W. Kong, G. Li, M. Zou, D. Wang, Z. You, and X. Zhou, "Sparsity-based continuous wave terahertz lens-free on-chip holography with sub-wavelength resolution," Opt. Express **27**, 702–713 (2019).
24. K. Xue, Q. Li, Y. D. Li, and Q. Wang, "Continuous-wave terahertz in-line digital holography," Opt. Lett. **37**, 3228–3230 (2012).
25. L. Rong, T. Latychevskaia, D. Wang, X. Zhou, H. Huang, Z. Li, and Y. Wang, "Terahertz in-line digital holography of dragonfly hindwing: amplitude and phase reconstruction at enhanced resolution by extrapolation," Opt. Express **22**, 17236–17245 (2014).
26. L. Rong, T. Latychevskaia, C. Chen, D. Wang, Z. Yu, X. Zhou, Z. Li, H. Huang, Y. Wang, and Z. Zhou, "Terahertz in-line digital holography of human hepatocellular carcinoma tissue," Sci. Rep. **5**, 8445 (2015).
27. M. Yamagiwa, T. Minamikawa, F. Minamiji, T. Mizuno, Y. Tokizane, R. Oe, H. Koresawa, Y. Mizutani, T. Iwata, H. Yamamoto, and T. Yasui, "Visualization of internal structure and internal stress in visibly opaque objects using full-field phase-shifting terahertz digital holography," Opt. Express **27**, 33854–33868 (2019).
28. D. Wang, Y. Zhang, L. Rong, D. Ma, J. Zhao, and Y. Wang, "Continuous-wave terahertz self-referencing digital holography based on Fresnel's mirrors," Opt. Lett. **45**, 913–916 (2020).
29. M. Locatelli, M. Ravaro, S. Bartalini, L. Consolino, M. S. Vitiello, R. Cicchi, F. Pavone, and P. De Natale, "Real-time terahertz digital holography with a quantum cascade laser," Sci. Rep. **5**, 13566 (2015).
30. M. Yamagiwa, T. Ogawa, T. Minamikawa, D. G. Abdelsalam, K. Okabe, N. Tsurumachi, Y. Mizutani, T. Iwata, H. Yamamoto, and T. Yasui, "Real-time amplitude and phase imaging of optically opaque objects by combining full-field off-axis terahertz digital holography with angular spectrum reconstruction," J. Infrared Millim. Terahertz Waves **39**, 561–572 (2018).
31. D. Wang, Y. Zhao, L. Rong, M. Wan, X. Shi, Y. Wang, and J. T. Sheridan, "Expanding the field-of-view and profile measurement of covered objects in continuous-wave terahertz reflective digital holography," Opt. Eng. **58**, 023111 (2019).
32. M. Heimbeck and H. Everitt, "Terahertz digital holographic imaging," Adv. Opt. Photon. **12**, 1–59 (2020).
33. C. Wagner, S. Seebacher, W. Osten, and W. Jüptner, "Digital recording and numerical reconstruction of lensless Fourier holograms in optical metrology," Appl. Opt. **38**, 4812–4820 (1999).
34. M. Kumar and C. Shakher, "Experimental characterization of the hygroscopic properties of wood during convective drying using digital holographic interferometry," Appl. Opt. **55**, 960–968 (2016).
35. E. B. Malm, N. C. Monserud, C. G. Brown, P. W. Wachulak, H. Xu, G. Balakrishnan, W. Chao, E. Anderson, and M. C. Marconi, "Tabletop single-shot extreme ultraviolet Fourier transform holography of an extended object," Opt. Express **21**, 9959–9966 (2013).
36. M. M. Hossain, G. Sheoran, V. Kumar, and C. Shakher, "Contouring of diffused objects using lensless Fourier transform digital Moiré holography," Appl. Opt. **51**, 5331–5339 (2012).
37. A. Anand, A. Faridian, V. K. Chhaniwal, S. Mahajan, V. Trivedi, S. K. Dubey, G. Pedrini, W. Osten, and B. Javidi, "Single beam Fourier transform digital holographic quantitative phase microscopy," Appl. Phys. Lett. **104**, 103705 (2014).
38. S. Agarwal, V. Kumar, and C. Shakher, "Temperature measurement of wick stabilized micro diffusion flame under the influence of magnetic field using digital holographic interferometry," Opt. Laser Eng. **102**, 161–169 (2018).
39. J. W. Goodman, *Introduction to Fourier Optics*, 3rd ed. (Robert & Company, 2005), pp. 126–165.
40. P. Ferraro, S. De Nicola, A. Finizio, G. Coppola, S. Grilli, C. Magro, and G. Pierattini, "Compensation of the inherent wave front curvature in digital holographic coherent microscopy for quantitative phase-contrast imaging," Appl. Opt. **42**, 1938–1946 (2003).
41. M. D. Pritt and J. S. Shipman, "Least-squares two-dimensional phase unwrapping using FFT's," IEEE Trans. Geosci. Remote Sens. **32**, 706–708 (1994).
42. J. Di, J. Zhao, W. Sun, H. Jiang, and X. Yan, "Phase aberration compensation of digital holographic microscopy based on least squares surface fitting," Opt. Commun. **282**, 3873–3877 (2009).
43. M. Born and E. Wolf, *Principles of Optics* (Cambridge University, 1999), pp. 1–70.
44. C. Liu, Y. Li, X. Cheng, Z. Liu, F. Bo, and J. Zhu, "Elimination of zero-order diffraction in digital holography," Opt. Eng. **41**, 2434–2437 (2002).
45. F. J. Harris, "On the use of windows for harmonic analysis with the discrete Fourier transform," Proc. IEEE **66**, 51–83 (1978).
46. Y. Jin, G. Kim, and S. Jeon, "Terahertz dielectric properties of polymers," J. Korean Phys. Soc. **49**, 513–517 (2006).
47. M. Guizar-Sicairos, S. T. Thurman, and J. R. Fienup, "Efficient subpixel image registration algorithms," Opt. Lett. **33**, 156–158 (2008).
48. B. B. Hu and M. C. Nuss, "Imaging with terahertz waves," Opt. Lett. **20**, 1716–1718 (1995).
49. Z. Song, S. Yan, Z. Zhang, Y. Fu, D. Wei, H. Cui, and P. Lai, "Temporal and spatial variability of water status in plant leaves by terahertz imaging," IEEE Trans. Terahertz Sci. Technol. **8**, 520–527 (2018).
50. C. Jördens, M. Scheller, B. Breitenstein, D. Selmar, and M. Koch, "Evaluation of leaf water status by means of permittivity at terahertz frequencies," J. Biol. Phys. **35**, 255–264 (2009).
51. R. Gente and M. Koch, "Monitoring leaf water content with THz and sub-THz waves," Plant Methods **11**, 15 (2015).
52. L. Baldacci, M. Pagano, L. Masini, A. Toncelli, G. Carelli, P. Storchi, and A. Tredicucci, "Non-invasive absolute measurement of leaf water content using terahertz quantum cascade lasers," Plant Methods **13**, 51 (2017).
53. M. Izumi, H. Ishida, S. Nakamura, and J. Hidema, "Entire photodamaged chloroplasts are transported to the central vacuole by autophagy," Plant Cell **29**, 377–394 (2017).
54. H. B. Zhang, K. Mitobe, and N. Yoshimura, "Application of terahertz imaging to water content measurement," Jpn. J. Appl. Phys. **47**, 8065–8070 (2008).